

Article

A Lab on a Chip Experiment for Upscaling Diffusivity of Evolving Porous Media

Jenna Poonoosamy^{1,*}, Renchao Lu², Mara Iris Lönartz¹, Guido Deissmann¹, Dirk Bosbach¹
and Yuankai Yang¹

¹ Institute of Energy and Climate Research (IEK-6), Nuclear Waste Management and Reactor Safety, Forschungszentrum Jülich GmbH, 52425 Jülich, Germany; m.loenartz@fz-juelich.de (M.I.L.); g.deissmann@fz-juelich.de (G.D.); d.bosbach@fz-juelich.de (D.B.); y.yang@fz-juelich.de (Y.Y.)

² Helmholtz Centre for Environmental Research—UFZ, 04318 Leipzig, Germany; renchao.lu@ufz.de

* Correspondence: j.poonoosamy@fz-juelich.de

Abstract: Reactive transport modelling is a powerful tool to assess subsurface evolution in various energy-related applications. Upscaling, i.e., accounting for pore scale heterogeneities into larger scale analyses, remains one of the biggest challenges of reactive transport modelling. Pore scale simulations capturing the evolutions of the porous media over a wide range of Peclet and Damköhler number in combination with machine learning are foreseen as an efficient methodology for upscaling. However, the accuracy of these pore scale models needs to be tested against experiments. In this work, we developed a lab on a chip experiment with a novel micromodel design combined with operando confocal Raman spectroscopy, to monitor the evolution of porous media undergoing coupled mineral dissolution and precipitation processes due to diffusive reactive fluxes. The 3D-imaging of the porous media combined with pore scale modelling enabled the derivation of upscaled transport parameters. The chemical reaction tested involved the replacement of celestine by strontianite, whereby a net porosity increase is expected because of the smaller molar volume of strontianite. However, under our experimental conditions, the accessible porosity and consequently diffusivity decreased. We propose a transferability of the concepts behind the Verma and Pruess relationship to be applied to also describe changes of diffusivity for evolving porous media. Our results highlight the importance of calibrating pore scale models with quantitative experiments prior to simulations over a wide range of Peclet and Damköhler numbers of which results can be further used for the derivation of upscaled parameters.

Keywords: reactive transport modelling; Archie's law; microfluidic experiments; lattice Boltzmann simulation; porous media imaging



Citation: Poonoosamy, J.; Lu, R.; Lönartz, M.I.; Deissmann, G.; Bosbach, D.; Yang, Y. A Lab on a Chip Experiment for Upscaling Diffusivity of Evolving Porous Media. *Energies* **2022**, *15*, 2160. <https://doi.org/10.3390/en15062160>

Academic Editor:
Moghtada Mobedi

Received: 18 February 2022

Accepted: 14 March 2022

Published: 16 March 2022

Publisher's Note: MDPI stays neutral with regard to jurisdictional claims in published maps and institutional affiliations.



Copyright: © 2022 by the authors. Licensee MDPI, Basel, Switzerland. This article is an open access article distributed under the terms and conditions of the Creative Commons Attribution (CC BY) license (<https://creativecommons.org/licenses/by/4.0/>).

1. Introduction

Reactive transport modelling (RTM) has become a powerful and indispensable tool for predicting subsurface flow and transport processes in space and time for various energy-related applications including geothermal energy extraction [1], CO₂ sequestration [2,3], exploitation of natural gas reservoirs [4], or geological disposal of nuclear waste [5–7]. Although RTM can solve complex couplings between multi-phase fluid flow and mineralogical reactions [8], e.g., CO₂ gas injection into deep saline aquifers with feedbacks of mineralogical reactions on transport parameters [9], the empirical formulations to describe coupled processes are debated [10]. Indeed, RTM rationalizes the complex processes in porous media on a continuum-scale and considers a representative elementary volume [11] with the average chemical and transport properties of a rock, e.g., porosity and diffusivity, while the macroscopic behaviour of the system is controlled by pore scale features, e.g., pore connectivity and surface roughness of minerals. One of the big challenges of RTM is the development of constitutive equations for the effective transport properties of porous

media and the reactivity of minerals that can be integrated into continuum analyses, i.e., “upscaling” [12–14].

The effects of mineral dissolution and precipitation on transport parameters in RTM are considered via empirical constitutive equations, e.g., Archie’s law [15] for diffusivity and the Kozeny Carman equation [16] for permeability. Experimental benchmarks [17–21] conducted to test these implementations showed that these relationships underestimate the impact of precipitation processes on transport parameters. Pore scale modelling approaches, with the versatility to define the pore architecture of a rock matrix down to the nanometre scale [22], the mineralogical distribution at the grain scale including surface roughness [23], were developed to investigate how the pore structure is affected by dissolution [24,25] and precipitation processes [26–29]. Pore scale modelling has been applied to derive transport parameters and constitutive equations that describe transport properties of evolving porous media. For example, Deng et al. [30] conducted a series of numerical experiments to investigate the impact of celestine nucleation mechanisms, surface precipitation (heterogeneous nucleation) versus precipitation in pores (homogenous nucleation) on the transport properties of an inert porous medium. The study showed that classical Archie’s law cannot be applied for the studied system and proposed an extended law introducing the concept of critical porosity [31] and critical effective diffusivity, which refer to the inherent transport parameters of the altered porous medium after porosity clogging. To increase the efficiency of this approach, machine learning tools have been recently developed to parameterize constitutive equations [32,33]. The numerical datasets generated by pore scale modelling are used to train convolutional neural network models, which can then be further applied to derive constitutive equations. For example, Prasianakis et al. [34] used neural networks to investigate porosity–permeability relationships of a calcite containing porous medium undergoing dissolution. The numerical experiments covered a wide range of flow and reaction rate conditions, i.e., diverse Peclet and Damköhler numbers. Their model showed the inability of a single porosity–permeability relationship to be applied for the complete flow and reactivity conditions of the numerical experiments but instead proposed a fitted polynomial to characterize the permeability versus porosity evolution.

The derivation of constitutive transport equations is also possible by applying pore scale modelling on high quality images of the porous media. Steinwinder and Beckingham [35] applied pore scale modelling to X-ray tomography images of an Alberta Basin Sandstone that had undergone coupled mineral dissolution and precipitation to examine the impact of the variations of pore and pore throat size distributions on the evolution of porosity and permeability. The study highlighted the inappropriateness of the power law of the Kozeny Carman equation and proposed the Verma and Pruess relationship [36] or its extended version to reproduce the macroscopic permeability of the porous rock. The Verma and Pruess relationship introduces an additional parameter, the critical porosity, which in fact accounts for heterogeneities at the pore scale, e.g., localized clogging zones [37].

Various imaging methodologies have been developed for the visualization of reactive flows in porous media, including positron emission tomography [38], magnetic resonance imaging [37–39], and neutron tomography [40]. However, X-ray tomography is the most widely applied tool [3,41–43]. The principal reason is that beside conferring advantages such as non-invasive, non-destructive, and dynamic assessment of flow paths, it can also assess mineralogical changes. This identification is possible based on the attenuation coefficient of each material in the sampled material. While high atomic number containing minerals exhibit high attenuation and are therefore easily distinguishable, discerning lighter atoms containing minerals with similar densities can be challenging. For instance, a sandstone consisting of a mixture of calcite, gypsum, and quartz is complex to differentiate by X-ray tomography due to the very similar attenuation coefficients of the three minerals [44]. Recently the use of confocal Raman spectroscopy has been proposed as a non-destructive method to monitor the spatio-temporal evolution of porous media, e.g., assessing the effects of hydrological heterogeneities on nucleation mechanisms [45] or for identifying minerals during coupled dissolution and precipitation processes [46]. Given 4D capabilities and the

high spatial resolution of Raman imaging (~ 500 nm), mineral identification can be used as a complementary analytical tool to X-ray tomography when the identification of mineral phases using the latter is demanding.

The aim of this work is therefore to develop an experiment which employs confocal Raman spectroscopy to monitor transport coupled mineralogical reactions, enabling the up-scaling of diffusive transport parameters of evolving porous media. We focussed our study specifically on reactive media undergoing coupled mineral dissolution and precipitation as existing work so far have mostly tackled diffusion induced mineral precipitation [19–21,47]. Our experimental approaches follow the lab on a chip concept [45,48,49] whereby reactions occurring in microreactors are monitored by advanced analytical techniques.

2. Materials and Methods

2.1. Setup and Microreactor Design

The experimental setup consists of a microfluidic experiment monitored by high-resolution optical microscopy and confocal Raman spectroscopy. The micro-reactor was mounted on automated x-y-z stage and connected to a pump (NeMeSYS, Cetoni GmbH, Korbußen, Germany) and an effluent vessel as shown in Figure 1a. The 3D single use PDMS chip bonded to glass was designed and fabricated according to Poonosamy et al. [47], consisting of four microreactors (Figure 1b) [48]. The supply channel of $150\ \mu\text{m}$ width and a length of $12.7\ \text{mm}$ connects the inert porous medium (Figure 1c) to a reservoir filled with a reactive porous medium (Figure 1d).

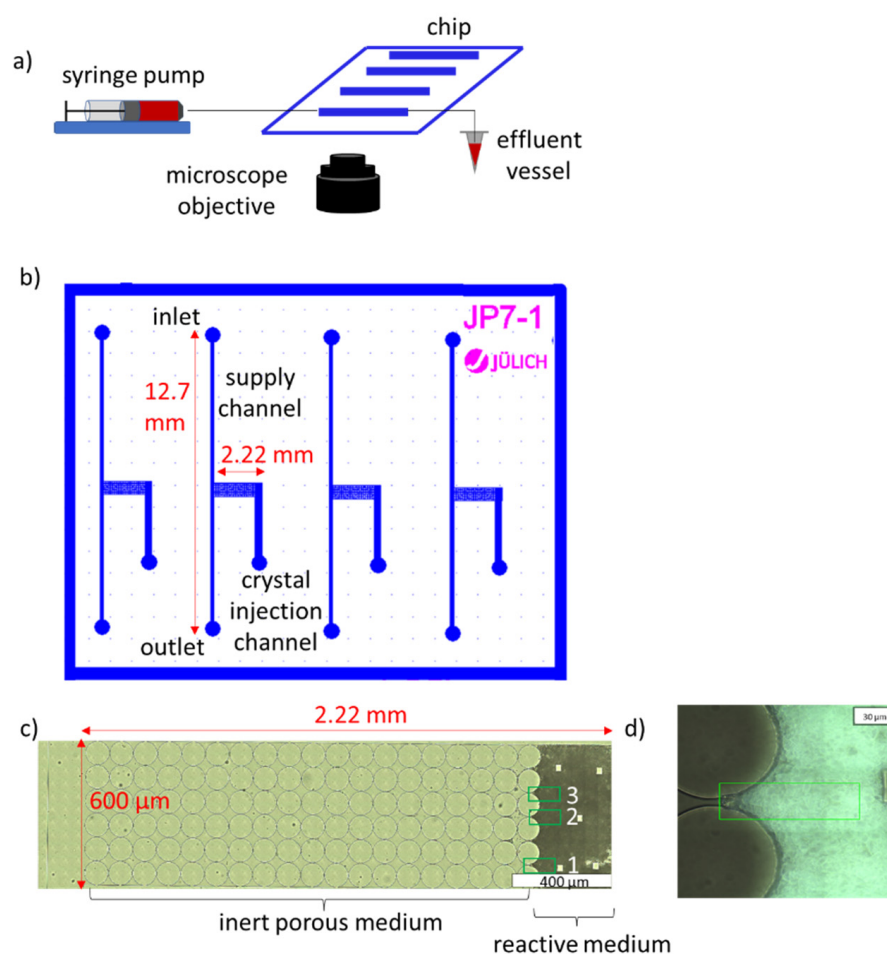
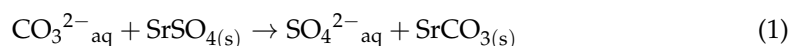


Figure 1. (a) Experimental setup; (b) chip design with (c) a zoom on the inert porous medium and (d) the reactive porous medium.

The inert porous medium was 1.92 mm long and 600 μm wide and consisted of an array of cylindrical pillars of 100 μm diameter distanced by 1 μm from each other. The reservoir had dimensions of 600 μm \times 300 μm with 5 squared pillars integrated to maintain mechanical support. The depth of each microreactor was 10 μm . The reservoir was filled with naturally occurring celestine (SrSO_4) crystals with low porosity crushed to a size of 4–9 μm (see Poonoosamy et al. [17] for analysis of purity). A suspension of the crystals was injected via the crystal injection channel following the seeding procedure developed in Poonoosamy et al. [45]. The crystals were trapped in the reservoir by the pillars (distance 1 μm to each other), which acted as a sieve. The reactors were filled with celestine with initial porosities between 0.60 to 0.92 (see video in Supplement Video S1) of which the initial effective diffusivities were determined using pore scale modelling (cf. Section 2.4). The reactor with an initial porosity adjusted to 0.92 (average value for three sampled locations) was used for the reactive transport experiment (cf. Section 2.2).

2.2. Chemical Reactions

A solution of 1 M of sodium hydrogen carbonate (NaHCO_3) at pH \sim 9.0 was injected in the supply channel at a flow rate of 800 nL min^{-1} for 24 h, leading to the following chemical reaction in the reactive porous medium:



The injection of the NaHCO_3 solution induces the dissolution of celestine and the precipitation of strontianite (SrCO_3) (Equation (1)), because of its much lower solubility product (cf. Table 1). This reaction is accompanied by an increase in “net porosity” (used in the following for porosity changes based solely on the molar volumes of the minerals involved) due to the smaller molar volume of strontianite ($3.901 \times 10^{-5} \text{ m}^3 \text{ mol}^{-1}$ [50]) compared to that of celestine ($4.625 \times 10^{-5} \text{ m}^3 \text{ mol}^{-1}$ [50]).

Table 1. Properties of the different zones and composition of the injected solution in the 1D continuum scale reactive transport simulation.

Zone	Properties
Q_a (inert porous medium)	length $1.9 \times 10^{-3} \text{ m}$ initial porosity, Φ , 0.21 volume fraction of inert matrix 0.79 $D_{e,initial}$ $2.1 \times 10^{-10} \text{ m}^2 \text{ s}^{-1}$ exponent (Equation (6)), $m = 1$
Q_b (intermediate zone)	length $5 \times 10^{-5} \text{ m}$ initial porosity, Φ , 0.19 volume fraction of celestine 0.1 volume fraction of inert matrix 0.71 $D_{e,initial}$ $1.9 \times 10^{-10} \text{ m}^2 \text{ s}^{-1}$ exponent (Equation (6)), $m = 1$
Q_c (reactive porous medium)	length $3 \times 10^{-4} \text{ m}$ initial porosity, Φ , 0.92 volume fraction of celestine 0.08 $D_{e,initial}$ $8.3 \times 10^{-10} \text{ m}^2 \text{ s}^{-1}$ exponent (Equation (6)), $m = 2.3$
concentration NaHCO_3 initial pH of porous medium temperature solubility product, K_{sp} , celestine [50] solubility product, K_{sp} , strontianite [50]	1 M with pH \sim 9 5.6 25 $^\circ\text{C}$ $2.24 \times 10^{-7} \text{ mol}^2 \text{ L}^{-2}$ $5.6 \times 10^{-10} \text{ mol}^2 \text{ L}^{-2}$

Prior to the injection of the reacting solution, the microreactor was purged with a saturated strontium sulphate solution for 24 h at a constant flow rate of 800 nL min^{-1} ,

during which the initial 3D representation of the reactive porous medium was collected using Raman spectroscopy (cf. Section 2.2). To prevent any reactions in the supply channel, pure water was injected at 800 nL min^{-1} for 30 min before injecting the reacting solution. The experiment was conducted at room temperature ($22 \text{ }^\circ\text{C}$).

2.3. Imaging and Raman Spectroscopy

The microfluidic experiment was monitored using an automated inverted microscope (WITec alpha300 Ri Inverted Confocal Raman Microscope, WITec Wissenschaftliche Instrumente und Technologie GmbH, Ulm, Germany) with a $100\times$ oil immersion objective with a numerical aperture (NA) of 1.25, working distance of 0.23 mm and cover glass correction for 0.17 mm from Nikon. The instrument is equipped with a Nd: YAG laser ($\lambda = 532.236 \text{ nm}$), a thermoelectrically cooled CCD Camera, and an ultra-high-throughput spectrometer UHTS300. The laser power was set to 30 mW and a grating with $1800 \text{ grooves mm}^{-1}$ was chosen, yielding a spectral resolution of 2 cm^{-1} . The theoretical, diffraction-limited lateral and axial resolutions of the Raman measurements at the sampled surface were $\sim 520 \text{ nm}$ and $\sim 2060 \text{ nm}$, respectively, considering Equations (3) and (4) in Everall [51], with a refraction index of the immersion medium of 1.51. The experimental setup is equipped with an enclosure to minimize interferences with room temperature fluctuations as well as cosmic rays.

Before the reaction, high resolution optical images of the compacted porous medium were taken, and the images were stitched for visualization of the structure of the reactive porous medium (Figure 1c,d). Three regions of interest (e.g., areas labelled 1 to 3 in Figure 1c) were selected and the mineralogical changes were monitored at regular time intervals using Raman spectroscopy. In situ hyperspectral Raman images were recorded from an area of $100 \text{ }\mu\text{m} \times 30 \text{ }\mu\text{m}$ with a 500 nm step size ($200 \text{ pixel} \times 60 \text{ pixel}$ per image) in x and y direction. The individual Raman spectra were collected during continuous x–y stage movement. Raman intensities were recorded for 0.1 s in the wavenumber range from 300 to 1300 cm^{-1} . The total exposure time was 25 min for a single image. In addition, stacked Raman images of the same size were collected over a depth of $11 \text{ }\mu\text{m}$ with a $1 \text{ }\mu\text{m}$ step size. These images were used to reconstruct the 3D geometry of the skeleton of the porous medium. The voxel resolution of our measurement is $500 \text{ }\mu\text{m}^3$. The heat introduced by the laser during the 3D Raman tomography has a negligible effect on the dissolution of celestine as discussed in Poonosamy et al. 2020 [45].

Raman image stacks were visualized with ImageJ 3D Viewer plugin³¹. An image processing workflow was developed using ImageJ to measure the porosity (voxel without minerals) and volume fraction of each mineral from the stacks. For that, each mineral phase was converted to greyscale levels and segmented by default thresholding into two classes of pixels (“foreground” and “background”). In addition, the images were converted into binary text files using Matlab to simulate the flow through the porous media (Section 2.5).

2.4. Velocity Field in the Microfluidic Reactor

The 3D flow field in the microfluidic device was simulated with computational fluid dynamics using the software COMSOL Multiphysics 5.6 (COMSOL AB, Stockholm, Sweden, see Appendix A). This step enables the characterization of the transport regime that prevails in the micromodel.

2.5. Numerical Tracer Experiment Using Pore Scale Modelling

The effective diffusivity of the unreacted and reacted porous media were determined using pore scale modelling. Numerical inert tracer experiments were conducted on the experimental 3D reactive porous medium collected by Raman imaging (Figure 2a; the intermediate section with pillars was removed for this analysis, i.e., the simulations addressed only the pure reactive porous media). For the reacted porous medium, it is known that solute transport can also occur through the newly formed precipitates [52,53] and therefore diffusion through the precipitates is considered in our numerical investigations.

The lattice Boltzmann method, LBM, which relies on the application of the Boltzmann transport equation to simulate fluid flow on discrete grids [54] was used for this purpose. Benefiting of the high efficiency of LBM for parallel computing, it has shown amazing performances to analyse fluid flow or heat and mass transfer in complex porous media during recent years [55,56].

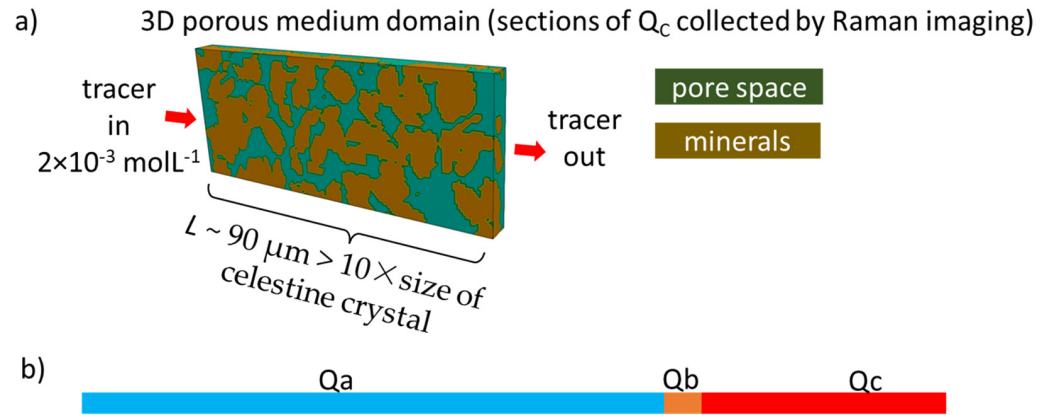


Figure 2. (a) An example of a 3D domain from Raman tomographs considered for numerical tracer experiments at the pore scale in Section 3.3; (b) 1D representation of domain considered for reactive transport simulation at the continuum scale in Section 3.4, with Q_a , Q_b , and Q_c representing the inert pillared porous medium, the intermediate zone with pillars and celestine, and finally the reactive porous medium, respectively.

We use LBM to solve the diffusion equation in the 3D porous media domains (from the Raman tomographs):

$$\frac{\partial C_p}{\partial t} = \nabla \cdot (D_i \cdot \nabla C_p) \quad (2)$$

where C_p denotes the local concentration of the inert tracer at pore scale. D_i is the local diffusion coefficient given by:

$$D_i = \begin{cases} D_0, & \text{in the electrolyte in the pores} \\ D_s, & \text{in the newly formed precipitates} \end{cases} \quad (3)$$

where D_0 is the tracer's diffusivity in free water and D_s its effective diffusivity in the precipitates forming the existing solids precipitations (i.e., strontianite in this experiment). A constant tracer concentration of 2 mM was applied at the inlet. When the process of tracer diffusion reaches a steady state, the effective diffusion coefficient, D_e [$\text{m}^2 \text{s}^{-1}$], can be calculated using the total mass flux J through the entire domain:

$$D_e = \frac{J \cdot L}{S(C_{in} - C_{out})} \quad (4)$$

with a length of the domain L [m] and a total cross-sectional area S [m^2]. Equations (2) and (4) are numerically solved by our previously developed framework based on LBM, which has been validated in these references [22,57].

For the evaluation of the effective diffusivity (D_e) of the reactive porous medium that had undergone mineral dissolution and precipitation, two numerical case studies were considered, case 1 without solute transport through the newly formed strontianite ($D_s = 0 \text{ m}^2 \text{ s}^{-1}$) and case 2 with transport through the newly formed precipitate ($D_s/D_0 = 0.01$). This factor, rounded to a 2-digit number, is calculated from Deng et al. [30], who fitted an inherent diffusivity of the precipitates of $5 \times 10^{-12} \text{ m}^2 \text{ s}^{-1}$ to match the experimental datasets of Chagneau et al. [19].

The correlation with the domain porosity, Φ , was also investigated for the derivation of a constitutive equation relating porosity and effective diffusivity.

2.6. Reactive Transport Model Setup at the Continuum Scale

In a final step, we aimed to compare the extended porosity-diffusivity model derived from 3D Raman images and pore scale modelling (Sections 2.3 and 2.5) with the classical Archie's law, which is applied to account for porosity changes due to mineralogical reactions on the solute diffusivity in the liquid phase. For this purpose, we conducted a 1D reactive transport simulation using the finite element package OpenGeoSys-6#Phreeqc [58,59], where an integration-point operator-splitting scheme [60] was used to solve the multi-species diffusion-reaction equations as follows [61,62]:

$$\frac{\partial(\Phi c_{T\alpha})}{\partial t} = \nabla \cdot (D_{e,\alpha} \nabla c_{T\alpha}) + R_{\alpha}^{\min}(c_{T1}, \dots, c_{Tm}), \quad (5)$$

where $c_{T\alpha}$ ($\alpha = 1, \dots, m$) (mol m^{-3}) is the total concentration of the α^{th} primary species in the liquid; $D_{e,\alpha}$ ($\text{m}^2 \text{s}^{-1}$) is the effective diffusion coefficient of the primary species α (assumed to have the same value for all the species in our model); and $R_{\alpha}^{\min}(c_{T1}, \dots, c_{Tm})$ is the heterogeneous reaction term accounting for the contributions of all mineral dissolution-precipitation reactions that involve the primary species α .

The computational domain consists of three zones (Figure 2b). The leftmost zone Q_a is made up of an inert pillared porous medium with a porosity of 0.21. The rightmost celestine-containing reservoir Q_c has a porosity of 0.92. The intermediate $50 \mu\text{m}$ zone, Q_b , consisting of pillars with stacked crystals, has a porosity of 0.19. A 1 M NaHCO_3 solution ($\text{pH} \sim 9$) was allowed to diffuse through the microfluidic device into the reacting reservoir represented by Q_c . In Table 1, the properties of the porous media in the different zones and the prescribed boundary conditions are summarized. The entire domain was evenly discretized using linear line elements with a grid spacing of $50 \mu\text{m}$. A fixed time step size of 0.2 s was used in the implicit backward Euler scheme.

Usually, the effective diffusion coefficient D_e is parameterized as a function of porosity. In this simulation, we use the classical Archie's law [15] to parameterize the effective diffusion coefficient [19]:

$$D_e = D_p \Phi^m, \quad (6)$$

where D_p is the pore diffusion coefficient set to $1 \times 10^{-9} \text{ m}^2 \text{ s}^{-1}$, Φ [-] is the porosity, and m [-] is an empirical coefficient. In this study, m was set to 1 for the inert zone (Q_a) and the intermediate zone (Q_b) and to 2.3 (a fitted value for a sandy compacted porous medium [19]) for the reactive porous medium in zone Q_c .

In our continuum scale simulations, we used a simple reaction system where the dissolving celestine and precipitating strontianite were assumed to equilibrate simultaneously against the incoming solution (i.e., as soon as oversaturation is reached). The PSI/NAGRA 12/07 chemical thermodynamic database (summarized in Table 3 in [63]) was used for the speciation calculation.

3. Results

3.1. Evaluation of Velocity Field

The injection of the NaHCO_3 solution in the supply channels at constant rate yields a velocity field at steady state as shown in Figure 3a. The velocity is highest at $\sim 1.2 \times 10^{-3} \text{ m s}^{-1}$ in the solution supply channels and decreases to $\sim 10^{-13} \text{ m s}^{-1}$ in the inert porous medium (i.e., left end of the Q_a region). The Peclet number (P_e , defined as the ratio of advective to diffusive transport rates) in the inert porous medium close to the reservoir was evaluated at 0.0001, with the consideration of a characteristic length of $1000 \mu\text{m}$ (i.e., a length over which the velocity is in the same order of magnitude). It can thus be inferred that diffusion dominates the transport of the reacting solutes into the reactive porous medium. Figure 3b shows the simulated concentration of sodium (Na, conservative solute transport) across

the porous media with time. Thus, it takes three hours for a steady sodium concentration gradient to be established across the inert porous medium.

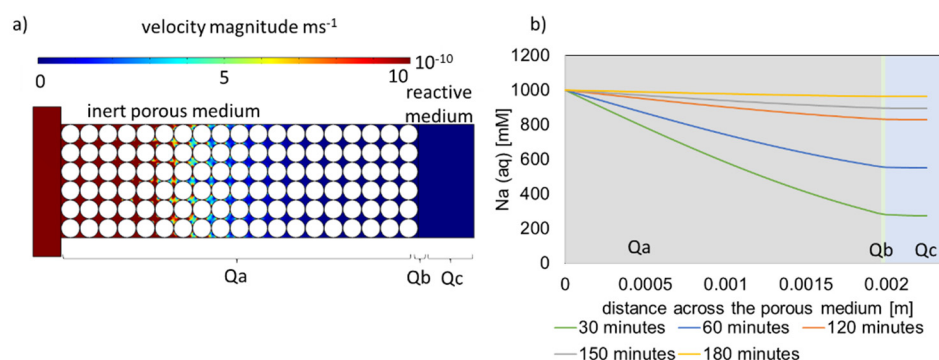


Figure 3. (a) 2D velocity map in the microfluidic device simulated using COMSOL Multiphysics (the upper limit of the scale bar was set at $10 \times 10^{-10} \text{ m s}^{-1}$ for a better visualization of the velocities in the inert porous medium); (b) simulated concentration of total aqueous sodium across the reactor using OpenGeosys-6#Phreeqc as function of time.

3.2. Mineralogical and Porosity Changes

The mineral phases in the reservoir were identified by the characteristic Raman-active modes. The spectra of strontianite and celestine are distinct. Figure 4a shows the temporal evolution of the distribution of celestine (identified in red) and newly formed strontianite (identified in yellow) in the three sampled areas labelled 1 to 3 (cf. Figure 1c). The dissolution of celestine followed by precipitation of strontianite is a fast process with only $14 \pm 4\%$ of the initial celestine remaining undissolved after 6 h of reaction (Figure 4b) and a complete replacement observed within 10 h. From the Raman images, precipitates were observed to initiate on the surface of larger crystals of celestine (e.g., in area i in Figure 4a) and as a very fine “fluffy” precipitate that recrystallizes into larger crystals (e.g., in area ii in Figure 4a). No precipitation was observed in the inert porous medium.

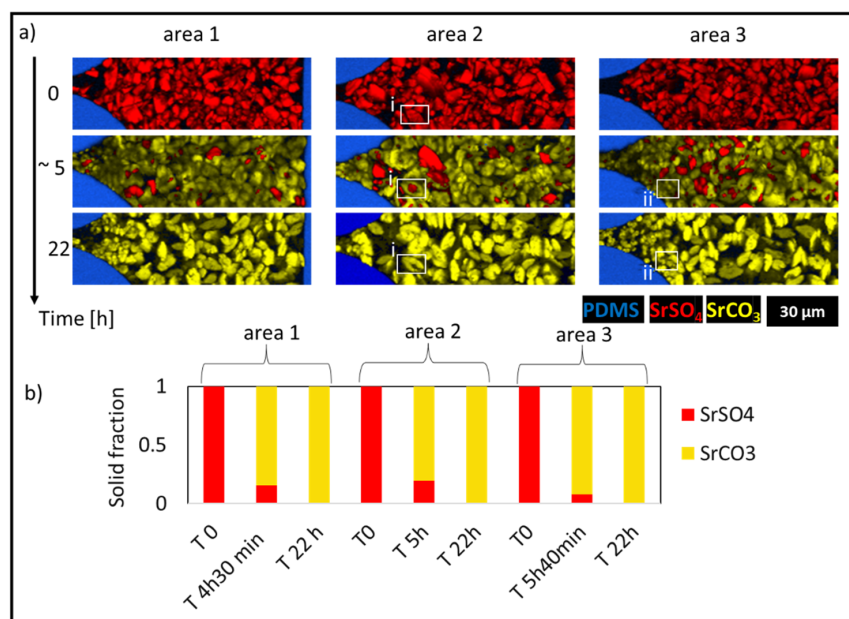


Figure 4. (a) 2D Raman images capturing the mineralogical changes in the monitored areas with time with interface coupled dissolution and precipitation (ICDP) with the formation of encrustation pseudomorphs (i) and recrystallization of the fine grain strontianite (Oswald ripening, (ii)); (b) mole fractions of the initial celestine converted to strontianite.

The accessible porosities, which we defined as the fraction of voxels unoccupied by minerals before and after reaction were calculated from the 3D Raman tomographic images of the porous media (Figure 5a) and are given in Figure 5b. The volume occupied by the newly formed precipitates is larger than the pristine celestine crystal (see video in Supplement Video S2). Thus, the average measured “accessible” porosity of the reacted porous medium decreases to ~ 0.54 . In contrast, based on the difference in molar volume between celestine and strontianite, the final porosity or “net porosity” should increase from ~ 0.92 to ~ 0.93 . Hence, the replacement of celestine by strontianite involves an increase in net porosity but a decrease in accessible porosity for transport.

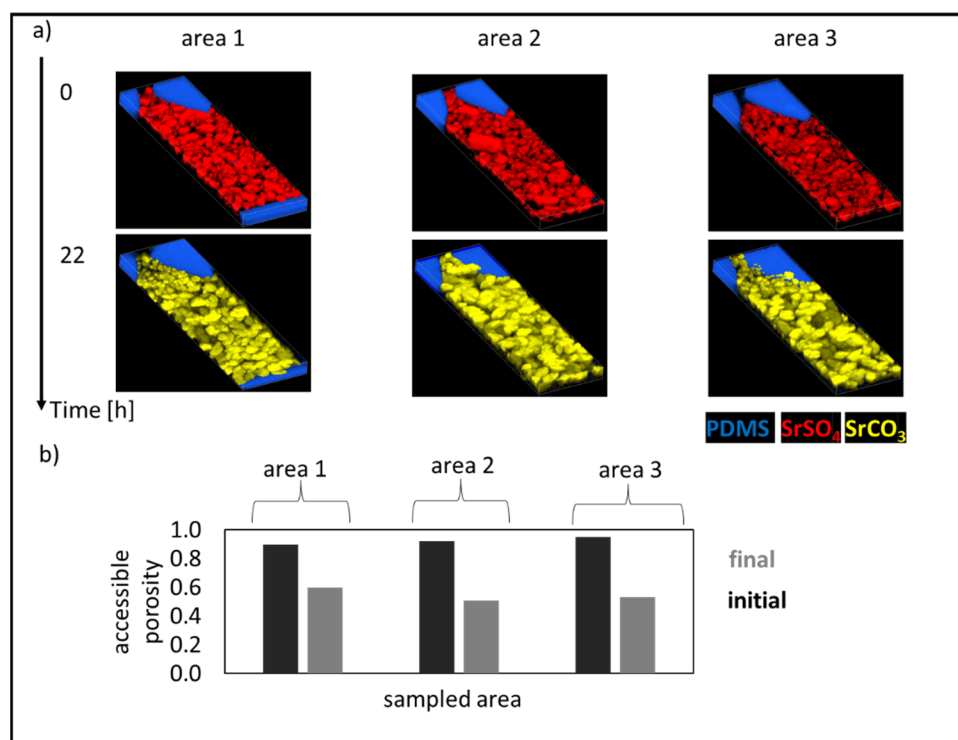


Figure 5. (a) Initial and final Raman tomographs of the sampled areas, and (b) the associated porosity changes.

3.3. Evaluation of the Effective Diffusivity

The tracer concentration in the reactive porous medium before and after reaction simulated using the lattice Boltzmann method is shown in Figure 6. The tracer concentration map across the domain before and after coupled dissolution and precipitation indicates a new pore architecture, whereby the final effective diffusivity is lower by a factor of ~ 0.5 (averaged for the three areas) as the initial effective diffusivity. When diffusion is allowed through the newly formed strontianite with $D_s/D_0 = 0.01$ (Figure 6c), this factor increases slightly to 0.52 (averaged for the three areas). In addition, sensitivity analyses, with D_s/D_0 equal to 0.04 and 0.1 were conducted. All simulated results indicated a decrease in the effective diffusivity of the reacted porous medium with the being less pronounced as D_s/D_0 increases (see tabulated datasets in Appendix C).

The correlation between the simulated effective diffusivities and the calculated porosities from the 3D images is shown in Figure 7. For the unreacted porous media of porosities between 0.60 to 0.92, the associated diffusivities are indicated on the graph by the red data points. Our analysis shows that Archie’s law parameterized for compacted sandy porous material reproduces well the simulated effective diffusion coefficient of the unreacted celestine medium at different porosities. In addition, we report the accessible porosities of the chemically altered media and the associated simulated effective diffusivities (grey data points in Figure 7). Here, the simulated effective diffusivities of the reacted porous media

are rather invariant with respect to the assumption regarding the diffusivity of the newly formed strontianite precipitates.

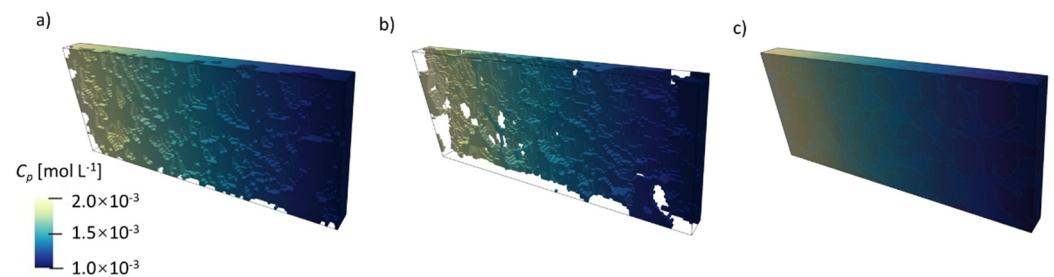


Figure 6. 3D view of the simulated tracer concentrations across the sampled porous media in (a) initial state (unreacted porous medium), (b) final state assuming no diffusion through the precipitates ($D_s = 0$), and (c) final state with diffusion through the precipitates with $D_s/D_0 = 0.01$.

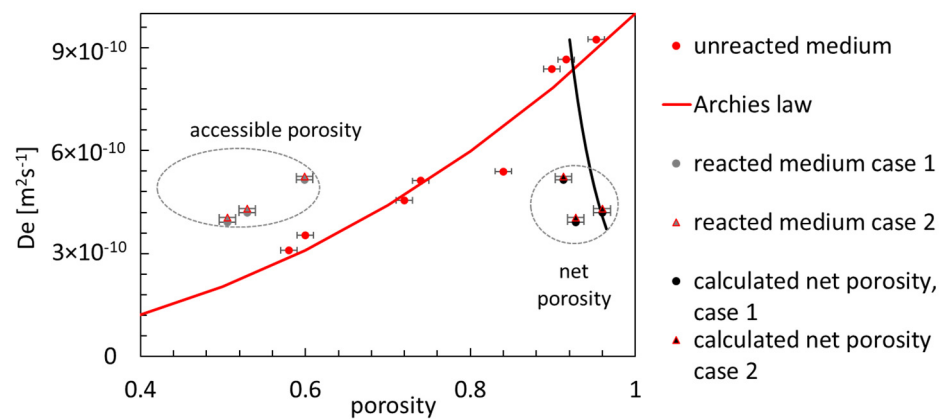


Figure 7. Graph relating porosities of sampled areas with effective diffusivities.

In a continuum scale reactive transport model, the changes in diffusivities due to mineralogical reactions can only be accounted for based on the net porosity changes calculated from changes in molar volumes. Consequently, the net porosities (black data points in Figure 7) have to be considered instead of the accessible porosities in continuum scale reactive transport simulations. Here, Archie's law fails to reproduce the experimental observations. Therefore, we tested an alternative approach for describing the porosity—diffusivity relationship. As mentioned earlier, Deng et al. [30] conducted a series of numerical experiments on diffusion induced precipitation of celestine and proposed the following porosity—diffusivity relationship:

$$D_e = D_{effc} + aD_p(\Phi - \Phi_c)^n, \quad (7)$$

where a and n are empirical coefficients, Φ_c and D_{effc} are defined as the critical porosity and effective diffusivity post porosity clogging, respectively. In our experiment, where no porosity clogging is observed, we can assume that $D_{effc} = 0$, and therefore the ratio of the initial ($D_{e,initial}$) and final ($D_{e,t}$) effective diffusivity can be simplified to:

$$\frac{D_{e,t}}{D_{e,initial}} = \left(\frac{\Phi_t - \Phi_c}{\Phi_0 - \Phi_c} \right)^n, \quad (8)$$

where $D_{e,initial}$ and Φ_0 are the initial diffusivity and porosity, respectively. Φ_c and n are fitted to 0.65 and -6 , respectively, to match the experimental data sets.

3.4. Reactive Transport Simulation at the Continuum Scale

Reactive transport modelling at the continuum scale was performed to evaluate the impact of coupled celestine dissolution and strontianite precipitation and consequences on the diffusivity evolution, using (i) the classical Archie's law (Equation (6)) and (ii) using the extended diffusivity relationship (Equation (8)). The simulated mineralogical and associated porosity changes are the same for both studied cases and are presented in Figure 8a,b, respectively. The simulated mineralogical reactions with time are in good agreement with our experimental observations. The calculated Damköhler number, calculated using Equation (A2) in Appendix B, is around $\sim 10^5$ indicating that the system in our experimental conditions is controlled by the reaction given by the very high concentration of NaHCO_3 injected.

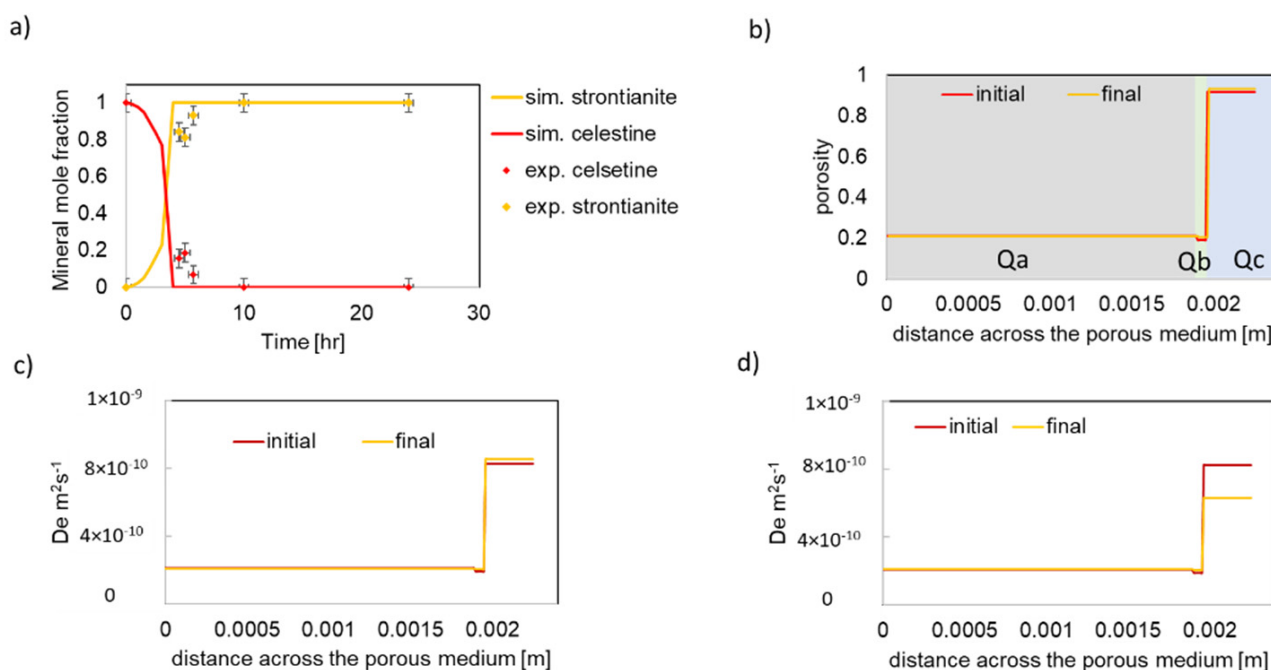


Figure 8. (a) Comparison between experimental and simulated temporal mineral reactions; (b) simulated initial and final net porosity across the porous medium (c) simulated diffusivity following Archie's law, and (d) following the extended law (Equation (8)).

Figure 8c,d show the simulated diffusive properties of the porous domain based on the two porosity-diffusivity models with a simulated diffusivity increase with Archie's law and a diffusivity decrease with the extended diffusivity relationship (Equation (8)).

In the current study, the use of Archie's law and the extended law had little impact of the simulated net mineralogical reactions within the considered domain and time scale. However, if the domain was extended to cm or m scale, differences between the mineralogical profiles and consequently porosity across the domain will develop.

4. Discussion

Archie's law parameterized to describe diffusion in a compacted sandy porous medium reproduces well the diffusivity of the unreacted celestine. When precipitation occurs, the precipitates cement the porous media creating a new pore architecture and the parameterized Archie's law is no more valid. The replacement of celestine by strontianite caused an unexpected decrease in accessible porosity which suggested that the newly formed precipitates were porous. The volume increase can be explained by the presence of fluid inclusions which are common for minerals precipitating at high saturation ratios [64,65], here calculated ~ 700 (cf. Appendix B for definition) and by the precipitation patterns. At high saturation ratios, both homogeneous (HON) and heterogeneous (HEN) nucleation can

occur at competitive rates ($9 \times 10^{22} \text{ m}^3 \text{ s}^{-1}$ for HON versus $2 \times 10^{19} \text{ m}^3 \text{ s}^{-1}$ for HEN using equations given in Appendix B) [66]. Heterogeneous nucleation of celestine appears to be favoured on the larger celestine crystals. This process, termed interface coupled dissolution and precipitation [67,68], can lead to the formation of encrustation pseudomorphs [17] (cf. area i in Figure 4a), i.e., a crystal with a void inside occupying more pore space than the original celestine crystal. On the other hand, the dissolution of the smaller celestine crystals can be a source of Sr^{2+} to fuel homogeneous nucleation. HON resulted in the formation of the fine “fluffy” strontianite phase (cf. area ii in Figure 4a). The very fine strontianite seemed to undergo Oswald ripening forming larger cemented strontianite crystals, creating a new pore architecture. As such, the precipitation patterns can significantly reduce the experimentally measured accessible porosity and consequently the simulated diffusivity. Similar observations were reported for celestine dissolution followed by barite precipitation [64].

The newly formed precipitate will still enable diffusion of solutes to the surface of the initial minerals because of its inherent porosity [29,52], nevertheless, overall, the effective diffusivity decreases. The presented replacement study highlights the complexity of predicting coupled dissolution and precipitation processes and associated changes in transport properties of porous media. A similar behaviour was observed by Sabo and Beckingham [69] during which a coupled dissolution and precipitation with a net porosity increase was accompanied by a decrease in permeability. The authors proposed the Verma and Pruess relationship combined with a negative exponent to rationalize their observations. The Verma and Pruess relationship has already proven to reproduce permeability changes due to coupled mineral dissolution and precipitation processes [17,69,70] and should be considered in continuum scale reactive transport modelling. In fact, the proposed Equation (8) to characterize diffusivity is an adaptation of the Verma and Pruess relationship. Currently, there exist no tabulation for the range of values taken by the critical porosity or the exponent for diffusive transport. However, the fitted values to match the presented experimental datasets are within the range reported by Hommel et al. [70] for describing permeability changes as consequence of altered porosity.

In addition to the properties of the initial porous medium, the parameterization of equations relating porosity to transport parameters is also known to depend on Peclet and Damköhler numbers [71–73]. To develop process based predictive models, a compilation of datasets for a wide range of Peclet and Damköhler numbers is necessary [73]. However, this might be a tedious work if such parameterizations are based solely on experiments. A more optimized approach is to calibrate pore scale models with a few reactive transport experiments at the same scale, which can point out the unexpected system behaviour. Afterwards, these calibrated models can then be used to simulate various flow and reaction conditions, extending datasets over a wide range of Peclet and Damköhler numbers. In the absence of experimental datasets on evolving porous media, it is important to include the extended law as sensitivity case when modelling real-world larger scale problems, which should set a range of uncertainty of the coupled reactive transport modelling.

5. Conclusions

We developed a lab on a chip experiment to monitor and upscale transport parameters of evolving porous media. Our experiment, involving the replacement of celestine by strontianite, yielded a net porosity increase but a decrease in accessible porosity for transport and consequently diffusive transport. Conventional Archie’s law failed to reproduce the experimental results, but rather an extended law based on the concept of the Verma and Pruess relationships was applied to reproduce the experimental observations.

The presented micromodel design can be used to assess coupled dissolution precipitation processes in a diffusive transport regime. The replacement process of celestine by strontianite can be easily identified by 3D Raman tomographic imaging, overcoming the more challenging identification by X-ray tomography [74]. The evolution of the pore architecture was captured at a voxel resolution of $0.5 \mu\text{m}^3$ which could even be improved to

$0.3 \mu\text{m}^3$ with an objective of 1.4 numerical aperture. Such an experiment can be carried out at elevated temperatures using a heating stage. Moreover, the presented chip design can be used to image the gas phase in variably saturated reactive porous media or for monitoring two phase flow systems [75]. Future work will focus on the development of microfluidic experiments combined with an automated image analysis and pipeline to a flow solver for the derivation of upscaled transport parameters using neural network.

Supplementary Materials: The following are available online at <https://www.mdpi.com/article/10.3390/en15062160/s1>, Video S1: Raman tomograph of initial reactive porous medium compacted to different porosities, Video S2: Visualization of the evolving porous media.

Author Contributions: J.P. designed the chip, designed and conducted the experiments, and analysed the Raman experimental datasets. R.L. implemented a new porosity-diffusivity relationship in OGS-PhreeqC and conducted the continuum scale modelling. Y.Y. conducted the pore scale modelling. M.I.L. performed the 3D image analysis. D.B., G.D. and J.P. contributed to the funding acquisition. All authors discussed the results and contributed to the writing/editing of the manuscript. All authors have read and agreed to the published version of the manuscript.

Funding: The research leading to these results has received funding from the German Federal Ministry of Education and Research (BMBF, grant agreement 02NUK053A) and from the Initiative and Networking Fund of the Helmholtz Association (HGF grant SO-093) within the iCross project. This research has received funding from the European Union's Horizon 2020 research and innovation programme under grant agreement No. 847593 (EURAD) within work package DONUT.

Institutional Review Board Statement: Not applicable.

Informed Consent Statement: Not applicable.

Data Availability Statement: The data presented in this study are available on request from the corresponding author.

Acknowledgments: J.P. is thankful to the team of Dietrich Kohlheyer (IBG-1, FZJ) for fabricating the silicon waver and Kathy Dahmen (IEK-6, FZJ) for technical support.

Conflicts of Interest: The authors declare no conflict of interest.

Appendix A

Numerical simulations were used to assess the local streamlines and velocity magnitudes in the multifluidic reactor. The transport equations were solved using the computational fluid dynamics software COMSOL Multiphysics 5.6 (COMSOL AB, Stockholm, Sweden). The velocity field in the reactor was calculated using the Navier–Stokes equation for laminar flow of an isothermal, incompressible and Newtonian fluid:

$$\rho u \cdot \nabla u = -\nabla p + \mu \nabla^2 u \quad ; \quad \nabla \cdot u = 0 \quad (\text{A1})$$

where u is the velocity vector, ρ and μ are the density and viscosity of the fluid (water) set to 1000 kg m^{-3} and $8.90 \times 10^{-4} \text{ Pa s}$, respectively. A no-slip condition was applied to the glass and PDMS walls of the reactor and a laminar inflow with a flow rate of 800 nL min^{-1} was specified for the supply channel inlet. A reference pressure of 0 Pa was applied at the outlet.

Appendix B

The Damköhler number is given as [76]:

$$D_a = \frac{\tau_{\text{transport}}}{\tau_{\text{reaction}}} = \frac{L^2}{\frac{D_e}{c} r}, \quad (\text{A2})$$

where $\tau_{transport}$ and $\tau_{reaction}$ are the transport and reaction time, respectively, L is the transport length, D_e is the effective diffusivity, c is the equilibrium concentration of SrCO_3 [$\text{mol kg}_{\text{water}}^{-1}$] and r is the reaction rate [$\text{mol kg}_{\text{water}}^{-1} \text{s}^{-1}$].

The saturation ratio, Ω , is the ratio of the ion activity product in solution divided by the solubility product; for SrCO_3 it is calculated using the equation below:

$$\Omega = \frac{\{\text{Sr}^{2+}\} \{\text{CO}_3^{2-}\}}{K_{\text{sp}}^0}, \quad (\text{A3})$$

where $\{\text{Sr}^{2+}\}$ and $\{\text{CO}_3^{2-}\}$ are the activities of strontium and sulphate ions in solution, respectively, and K_{sp}^0 is the solubility product constant of strontianite.

The nucleation rate depends on the saturation ratio and can be calculated as follows:

$$J = r \exp\left(-\frac{\Delta G_c}{kT}\right), \quad (\text{A4})$$

where k is the Boltzmann constant, T is the absolute temperature (298.15 K), r a pre-exponential factor related to the solubility and ΔG_c is the energy required for the formation of a nucleus of critical size. ΔG_c is given as:

$$\Delta G_c = \frac{\beta v_0^2 \sigma^3}{(kT \ln \Omega)^2}, \quad (\text{A5})$$

where v_0 is the molecular volume in the solid phase ($5.29 \times 10^{-29} \text{ m}^3$ for strontianite), β is a geometry factor that depends on the shape of the nucleus and was set to 16.8 (value for spheres according to Nielsen, 1967), and σ (J m^{-2}) is the specific surface energy of the cluster/solution interface set to 85 mJm^{-2} , the value for celestine (Schindler, 1967), since literature data is not available for strontianite. Only to justify this step, the surface tension for barite and witherite are 135 and 115 mJm^{-2} , respectively.

The pre-exponential factor, r , includes a volume diffusion step and is given as:

$$r = 2\pi Z D N_0 N_1 d_c \quad (\text{A6})$$

where D is the diffusion coefficient of SrCO_3 monomers set to $9.3 \times 10^{-10} \text{ m}^2 \text{ s}^{-1}$ and $d_c = \frac{4\sigma v}{kT \ln \Omega}$. N_1 and N_0 are concentrations that represent the number of monomers per unit volume of fluid and the number of nucleation sites, respectively. N_0 (HON) for homogeneous nucleation was set to $3.3 \times 10^{28} \text{ m}^{-3}$ and N_0 (HEN) for heterogeneous nucleation was set to $2.5 \times 10^{13} \text{ m}^{-3}$. N_1 depends on supersaturation and was evaluated using GEMS.

Z is the Zeldovich factor given as:

$$Z = \sqrt{\left(\frac{\Delta G_c}{3\pi kT (n_c)^2}\right)} \quad (\text{A7})$$

with the number of monomers in the critical nucleus, n_c , given as:

$$n_c = \left(\frac{2\sigma a}{3kT \ln \Omega}\right)^3 \quad (\text{A8})$$

where $a = 6.81 \times 10^{-19} \text{ m}^2$ is the area occupied by a molecule of SrCO_3 .

In the case of 3D nucleation, σ is replaced by an effective specific surface energy σ_{eff} (J m^{-2}) given as:

$$\sigma_{\text{eff}} = \Psi^{\frac{1}{3}}(\theta) \gamma \quad (\text{A9})$$

where $\Psi(\theta) = \left(\frac{1}{4}\right)(2 + \cos\theta)(1 - \cos\theta)^2$. n_c and the pre-exponential factor, τ , were re-evaluated accordingly. The contact angle was set to 30° in our calculation (typical values for mineral overgrowth [77]).

Figure A1 shows that under our experimental condition at SI 2.86, i.e., log of Ω , homogenous nucleation rate is higher than heterogenous nucleation rate.

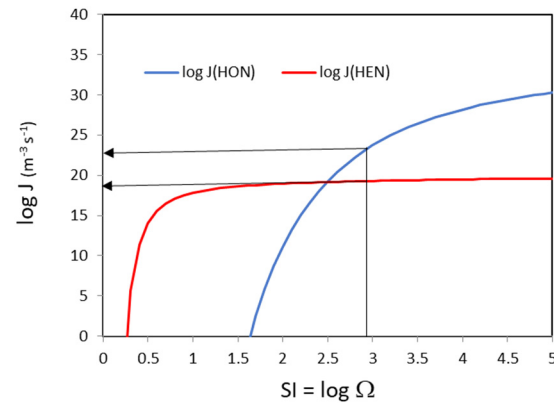


Figure A1. Graph comparing the homogenous versus heterogenous nucleation rate under our experimental conditions.

Appendix C

Tabulated porosities and associated effective diffusivities of the reactive porous media according to a sensitivity analysis with different D_s/D_0 ratios. Initial and final porosities were experimentally determined by 3D Raman tomography; the associated effective diffusivities were derived from pore scale modelling.

Case Study	Initial Porosity ± 0.01	D_e/D_0 (Initial)	Final Accessible Porosity ± 0.01	D_s/D_0	D_e/D_0 (Final)	$D_{e,final}/D_{e,initial}$
1	0.90	0.84	0.5993	0	0.51	0.607
1	0.92	0.87	0.5057	0	0.39	0.448
1	0.95	0.92	0.5294	0	0.42	0.457
2	0.90	0.84	0.5993	0.01	0.53	0.631
2	0.92	0.87	0.5057	0.01	0.41	0.471
2	0.95	0.92	0.5294	0.01	0.43	0.467
3	0.90	0.84	0.5993	0.04	0.55	0.655
3	0.92	0.87	0.5057	0.04	0.44	0.506
3	0.95	0.92	0.5294	0.04	0.46	0.500
4	0.90	0.84	0.5993	0.1	0.59	0.702
4	0.92	0.87	0.5057	0.1	0.49	0.563
4	0.95	0.92	0.5294	0.1	0.51	0.554

References

- Tranter, M.; de Lucia, M.; Kühn, M. Numerical investigation of barite scaling kinetics in fractures. *Geothermics* **2021**, *81*, 102027. [CrossRef]
- Sin, I.; Corvisier, J. Multiphase multicomponent reactive transport and flow modeling. *Rev. Mineral. Geochem.* **2019**, *85*, 143–195.
- Noiriel, C.; Soulaire, C. Pore-scale imaging and modelling of reactive flow in evolving porous media: Tracking the dynamics of the fluid–rock Interface. *Transp. Porous Media* **2021**, *140*, 181–213. [CrossRef]
- Sin, I.; Lagneau, V.; Laurent, D.W.; Jerome, C. 2D simulation of natural gas reservoir by two-phase multicomponent reactive flow and transport—Description of a benchmarking exercise. *Math. Comput. Simul.* **2017**, *137*, 431–447. [CrossRef]
- Trincherio, P.; Cvetkovic, V.; Selroos, J.-O.; Bosbach, D.; Deissmann, G. Upscaling of radionuclide transport and retention in crystalline rocks exhibiting micro-scale heterogeneity of the rock matrix. *Adv. Water Resour.* **2020**, *142*, 103644. [CrossRef]
- Idiart, A.; Laviña, M.; Kosakowski, G.; Cochepein, B.; Meeussen, J.; Samper, J.; Mon, A.; Montoya, V.; Munier, I.; Poonosamy, J.; et al. Reactive transport modelling of a low-pH concrete/clay interface. *Appl. Geochem.* **2020**, *115*, 104562. [CrossRef]

7. Damiani, L.H.; Kosakowski, G.; Vinsot, A.; Churakov, S.V. Mont Terri HT Experiment: Modelling of gas transfer between a borehole and claystone. *Environ. Geotech.* **2021**. [[CrossRef](#)]
8. Steefel, C.I. Reactive transport at the crossroads. *Rev. Mineral. Geochem.* **2019**, *85*, 1–26. [[CrossRef](#)]
9. Ahusborde, E.; Amaziane, B.; Moulay, M.I. High performance computing of 3D reactive multiphase flow in porous media: Application to geological storage of CO₂. *Comput. Geosci.* **2021**, *25*, 2131–2147. [[CrossRef](#)]
10. Seigneur, N.; Mayer, K.U.; Steefel, C.I. Reactive transport in evolving porous media. *Rev. Mineral. Geochem.* **2019**, *85*, 197–238. [[CrossRef](#)]
11. Bear, J. *Advances in Transport Phenomena in Porous Media*; Springer: Dordrecht, The Netherlands, 1987.
12. Churakov, S.V.; Prasianakis, N.I. Review of the current status and challenges for a holistic process-based description of mass transport and mineral reactivity in porous media. *Am. J. Sci.* **2018**, *318*, 921–948. [[CrossRef](#)]
13. Prasianakis, N.I.; Gatschet, M.; Abbasi, A.; Churakov, S.V. Upscaling strategies of porosity-permeability correlations in reacting environments from pore-scale simulations. *Geofluids* **2018**, 9260603, 2018. [[CrossRef](#)]
14. Ladd, A.J.; Szymczak, P. Reactive flows in porous media: Challenges in theoretical and numerical methods. *Annu. Rev. Chem. Biomol. Eng.* **2021**, *12*, 543–571. [[CrossRef](#)] [[PubMed](#)]
15. Archie, G.E. The electrical resistivity log as an aid in determining some reservoir characteristics. *Trans. Am. Inst. Min. Metall. Eng.* **1942**, *146*, 54–62. [[CrossRef](#)]
16. Carman, P.C. Fluid flow through granular beds. *Trans. Inst. Chem. Eng.* **1937**, *15*, 150–166. [[CrossRef](#)]
17. Poonoosamy, J.; Klinkenberg, M.; Deissmann, G.; Brandt, F.; Bosbach, D.; Mader, U.; Kosakowski, G. Effects of solution supersaturation on barite precipitation in porous media and consequences on permeability: Experiments and modelling. *Geochim. Cosmochim. Acta* **2020**, *270*, 43–60. [[CrossRef](#)]
18. Poonoosamy, J.; Kosakowski, G.; van Loon, L.R.; Mäder, U. Dissolution-precipitation processes in tank experiments for testing numerical models for reactive transport calculations: Experiments and modelling. *J. Contam. Hydrol.* **2015**, 1–17, 177–178. [[CrossRef](#)] [[PubMed](#)]
19. Chagneau, A.; Claret, F.; Enzmann, F.; Kersten, M.; Heck, S.; Madé, B.; Schäfer, T. Mineral precipitation-induced porosity reduction and its effect on transport parameters in diffusion-controlled porous media. *Geochem. Trans.* **2015**, *16*, 1–16. [[CrossRef](#)] [[PubMed](#)]
20. Rajyaguru, A.; L'Hôpital, E.; Savoye, S.; Wittebroodt, C.; Bildstein, O.; Arnoux, P.; Detilleux, V.; Fatnassi, I.; Gouze, P.; Lagneau, V. Experimental characterization of coupled diffusion reaction mechanisms in low permeability chalk. *Chem. Geol.* **2019**, *503*, 29–39. [[CrossRef](#)]
21. Rajyaguru, A.; Wang, J.; Wittebroodt, C.; Bildstein, O.; Detilleux, V.; Lagneau, V.; Savoye, S. Barite precipitation in porous media: Impact of pore structure and surface charge on ionic diffusion. *J. Contam. Hydrol.* **2021**, *242*, 103851. [[CrossRef](#)]
22. Yang, Y.; Patel, R.A.; Churakov, S.V.; Prasianakis, N.I.; Kosakowski, G.; Wang, M. Multiscale modeling of ion diffusion in cement paste: Electrical double layer effects. *Cem. Concr. Compos.* **2022**, *96*, 55–65. [[CrossRef](#)]
23. Deng, H.; Molins, S.; Trebotich, D.; Steefel, C.; De Paolo, D. Pore-scale numerical investigation of the impacts of surface roughness: Upscaling of reaction rates in rough fractures. *Geochim. Cosmochim. Acta* **2018**, *239*, 374–389. [[CrossRef](#)]
24. Soulaïne, C.; Roman, S.; Kovscek, A.; Tchepeli, H.A. Pore-scale modelling of multiphase reactive flow: Application to mineral dissolution with production of CO₂. *J. Fluid Mech.* **2018**, *855*, 616–645. [[CrossRef](#)]
25. Prill, T.; Fischer, C.; Gavrilenko, P.; Iliev, O. Implementing the variability of crystal surface reactivity in reactive transport modeling. *Transp. Porous Media* **2021**, *140*, 535–557. [[CrossRef](#)]
26. Prasianakis, N.I.; Curti, E.; Kosakowski, G.; Poonoosamy, J.; Churakov, S.V. Deciphering pore-level precipitation mechanisms. *Sci. Rep.* **2017**, *7*, 13765. [[CrossRef](#)] [[PubMed](#)]
27. Patel, R.; Churakov, S.V.; Prasianakis, N.I. A multi-level pore scale reactive transport model for the investigation of combined leaching and carbonation of cement paste. *Cem. Concr. Compos.* **2021**, *115*, 103831. [[CrossRef](#)]
28. Nooraiepour, M.; Masoudi, M.; Hellevang, H. Probabilistic nucleation governs time, amount, and location of mineral precipitation and geometry evolution in the porous medium. *Sci. Rep.* **2021**, *11*, 16397. [[CrossRef](#)] [[PubMed](#)]
29. Varzina, A.; Cizer, Ö.; Yu, L.; Liu, S.; Jacques, D.; Perko, J. A new concept for pore-scale precipitation-dissolution modelling in a lattice Boltzmann framework—Application to portlandite carbonation. *Appl. Geochem.* **2020**, *123*, 104786. [[CrossRef](#)]
30. Deng, H.; Tournassat, C.; Molins, S.; Claret, F.; Steefel, C. A pore-scale investigation of mineral precipitation driven diffusivity change at the column-scale. *Water Resour. Res.* **2021**, *57*, e2020WR028483. [[CrossRef](#)]
31. Navarre-Sitchler, A.; Steefel, C.; Yang, I.; Tomutsa, L.; Brantley, S. Evolution of porosity and diffusivity during chemical weathering of a basalt clast. *J. Geophys. Res.* **2009**, *114*, F02016.
32. Wu, H.; Fang, W.-Z.; Kang, Q.; Tao, W.-Q.; Qiao, R. Predicting effective diffusivity of porous media from images by deep learning. *Sci. Rep.* **2019**, *9*, 20387. [[CrossRef](#)] [[PubMed](#)]
33. Menke, H.; Maes, J.; Geiger, S. Upscaling the porosity–permeability relationship of a microporous carbonate for Darcy-scale flow with machine learning. *Sci. Rep.* **2021**, *11*, 2625. [[CrossRef](#)] [[PubMed](#)]
34. Prasianakis, N.I.; Haller, R.; Mahrous, M.; Poonoosamy, J.; Pfingsten, W.; Churakov, S.V. Neural network based process coupling and parameter upscaling in reactive transport simulations. *Geochim. Cosmochim. Acta* **2020**, *291*, 126–143. [[CrossRef](#)]
35. Steinwinder, J.; Beckingham, L.E. Role of pore and pore-throat distributions in controlling permeability in heterogeneous mineral dissolution and precipitation scenarios. *Water Resour. Res.* **2019**, *55*, 5502–5517. [[CrossRef](#)]

36. Verma, A.; Pruess, K. Thermohydrological conditions and silica redistribution near high level nuclear emplaced in saturated geological formation. *J. Geophys. Res.* **1988**, *93*, 1159–1173. [[CrossRef](#)]
37. Poonoosamy, J.; Haber-Pohlmeier, S.; Deng, H.; Deissmann, G.; Klinkenberg, M.; Gizatullin, B.; Stapf, S.; Brandt, F.; Bosbach, D.; Pohlmeier, A. Combination of MRI and SEM to assess changes in the chemical properties and permeability of porous media due to barite precipitation. *Minerals* **2020**, *10*, 226. [[CrossRef](#)]
38. Kulenkampff, J.; Stoll, M.; Gründig, M.; Mansel, A.; Lippmann-Pipke, J.; Kersten, M. Time-lapse 3D imaging by positron emission tomography of Cu mobilized in a soil column by the herbicide MCPA. *Sci. Rep.* **2018**, *8*, 7091. [[CrossRef](#)] [[PubMed](#)]
39. Markale, I.; Cimmarusti, G.M.; Britton, M.M.; Jiménez-Martínez, J. Phase saturation control on mixing-driven reactions in 3D porous media. *Environ. Sci. Technol.* **2021**, *55*, 8742–8752. [[CrossRef](#)] [[PubMed](#)]
40. Shafizadeh, A.; Gimmi, T.; van Loon, L.; Kaestner, A.; Mäder, U.; Churakov, S. Time-resolved porosity changes at cement-clay interfaces derived from neutron imaging. *Cem. Concr. Res.* **2021**, *127*, 105924. [[CrossRef](#)]
41. Agrawal, P.; Mascini, A.; Bultreys, T.; Aslannejad, H.; Wolthers, M.; Cnudde, V.; Butler, I.; Raoof, A. The impact of pore-throat shape evolution during dissolution on carbonate rock permeability: Pore network modeling and experiments. *Adv. Water Resour.* **2021**, *155*, 103991. [[CrossRef](#)]
42. Scanziani, A.; Singh, K.; Menke, H.; Bijeljic, B.; Blunt, M. Dynamics of enhanced gas trapping applied to CO₂ storage in the presence of oil using synchrotron X-ray micro tomography. *Appl. Energy* **2019**, *259*, 114136. [[CrossRef](#)]
43. Leger, M.; Luquot, L. Importance of microstructure in carbonate rocks: Laboratory and 3D-imaging petrophysical characterization. *Appl. Sci.* **2021**, *11*, 3784. [[CrossRef](#)]
44. Vlassenbroeck, J.; Cnudde, V.; Masschaele, B.; Dierick, M.; Hoorebeke, L.; Jacobs, P. A comparative and critical study of X-ray CT and neutron CT as non-destructive material evaluation techniques. *Geol. Soc. Lond. Spec. Publ.* **2007**, *271*, 277–285. [[CrossRef](#)]
45. Poonoosamy, J.; Soullaine, C.; Burmeister, A.; Deissmann, G.; Bosbach, D.; Roman, S. Microfluidic flow-through reactor and 3D Raman imaging for in situ assessment of mineral reactivity in porous and fractured porous media. *Lab Chip* **2020**, *20*, 2562–2571. [[CrossRef](#)] [[PubMed](#)]
46. Steefel, C.; Yang, L. Secondary magnesite formation from forsterite under CO₂ sequestration conditions via coupled heterogeneous nucleation and crystal growth. *Geochim. Cosmochim. Acta* **2021**, *311*, 29–42. [[CrossRef](#)]
47. Chagneau, A.; Tournassat, C.; Steefel, C.; Bourg, I.; Gaboreau, S.; Esteve, I.; Kupcik, T.; Claret, F.; Schäfer, T. Complete restriction of ³⁶Cl-diffusion by celestite precipitation in densely compacted illite. *Environ. Sci. Technol. Lett.* **2015**, *2*, 139–145. [[CrossRef](#)]
48. Poonoosamy, J.; Westerwalbesloh, C.; Deissmann, G.; Mahrous, M.; Curti, E.; Churakov, S.V.; Klinkenberg, M.; Kohlheyer, D.; Lieres, E.; Bosbach, D.; et al. A microfluidic experiment and pore scale modelling diagnostics for assessing mineral precipitation and dissolution in confined spaces. *Chem. Geol.* **2019**, *528*, 119264. [[CrossRef](#)]
49. Poonoosamy, J.; Mahrous, M.; Curti, E.; Bosbach, D.; Deissmann, G.; Churakov, S.; Geisler, T.; Prasianakis, N. A lab-on-a-chip approach integrating in-situ characterization and reactive transport modelling diagnostics to unravel (Ba,Sr)SO₄ oscillatory zoning. *Sci. Rep.* **2021**, *11*, 23678. [[CrossRef](#)] [[PubMed](#)]
50. Sverjensky, D.; Shock, E.; Helgeson, H. Prediction of the thermodynamic properties of aqueous metal complexes to 1000 °C and 5 kb. *Geochim. Cosmochim. Acta* **1997**, *61*, 1359–1412. [[CrossRef](#)]
51. Everall, N.J. Confocal Raman Microscopy: Performance, Pitfalls, and Best Practice. *Appl. Spectrosc.* **2009**, *63*, 245A–262A. [[CrossRef](#)]
52. Deng, H.; Poonoosamy, J.; Molins, S. A reactive transport modeling perspective on the dynamics of interface-coupled dissolution-precipitation. *Appl. Geochem.* **2022**, *137*, 105207. [[CrossRef](#)]
53. Luraschi, P.; Gimmi, T.; van Loon, L.; Shafizadeh, A.; Churakov, S. Evolution of HTO and ³⁶Cl—Diffusion through a reacting cement-clay interface (OPC paste-Na montmorillonite) over a time of six years. *Appl. Geochem.* **2020**, *119*, 104581. [[CrossRef](#)]
54. Chen, S.; Doolen, G.D. Lattice Boltzmann method for fluid flow. *Annu. Rev. Fluid Mech.* **1998**, *30*, 329–364. [[CrossRef](#)]
55. Yang, Y.; Wang, M. Cation diffusion in compacted clay: A pore-scale view. *Environ. Sci. Technol.* **2019**, *53*, 1976–1984. [[CrossRef](#)] [[PubMed](#)]
56. Wang, M.; Pan, N. Predictions of effective physical properties of complex multiphase materials. *Mater. Sci. Eng. R* **2008**, *63*, 1–30. [[CrossRef](#)]
57. Yang, Y.; Wang, M. Pore-scale modeling of chloride ion diffusion in cement microstructures. *Cem. Concr. Compos.* **2018**, *85*, 92–104. [[CrossRef](#)]
58. Kolditz, O.; Bauer, S.; Bilke, L.; Böttcher, N.; Delfs, J.O.; Fischer, T.; Görke, U.J.; Kalbacher, T.; Kosakowski, G.; McDermott, C.I.; et al. OpenGeoSys: An open-source initiative for numerical simulation of thermo-hydro-mechanical/chemical (THM/C) processes in porous media. *Environ. Earth Sci.* **2012**, *67*, 589–599. [[CrossRef](#)]
59. Parkhurst, D.; Appelo, C. *Description of Input and Examples for PHREEQC Version 3: A Computer Program for Speciation, Batch-Reaction, One-Dimensional Transport, and Inverse Geochemical Calculations*; U.S. Geological Survey: Denver, CO, USA, 2013.
60. Lu, R.; Nagel, T.; Poonoosamy, J.; Naumov, D.; Fischer, T.; Montoya, V.; Kolditz, O.; Shao, H. A new operator-splitting finite element scheme for reactive transport modeling in saturated porous media. *Comput. Geosci.* **2022**; *accepted manuscript*.
61. Kirkner, D.; Reeves, H. Multicomponent mass transport with homogeneous and heterogeneous chemical reactions: Effect of the chemistry on the choice of numerical algorithm: 1. Theory. *Water Resour. Res.* **1988**, *24*, 1719–1729. [[CrossRef](#)]
62. Steefel, C.; Lasaga, A. A coupled model for transport of multiple chemical species and kinetic precipitation/dissolution reactions with application to reactive flow in single phase hydrothermal systems. *Am. J. Sci.* **1994**, *294*, 529–592. [[CrossRef](#)]

63. Poonoosamy, J.; Wanner, C.; Epping, P.A.; Águila, J.F.; Samper, J.; Montenegro, L.; Xie, M.; Su, D.; Mayer, K.U.; Mäder, U.; et al. Benchmarking of reactive transport codes for 2D simulations with mineral dissolution–precipitation reactions and feedback on transport parameters. *Comput. Geosci.* **2021**, *25*, 1337–1358. [[CrossRef](#)]
64. Poonoosamy, J.; Curti, E.; Kosakowski, G.; van Loon, L.R.; Grolmund, D.; Mäder, U. Barite precipitation following celestite dissolution in a porous medium: A SEM/BSE and micro XRF/XRD study. *Geochim. Cosmochim. Acta* **2016**, *182*, 131–144. [[CrossRef](#)]
65. Weber, J.; Barthel, J.; Brandt, F.; Klinkenberg, M.; Breuer, U.; Kruth, M.; Bosbach, D. Nano-structural features of barite crystals observed by electron microscopy and atom probe tomography. *Chem. Geol.* **2016**, *424*, 51–59. [[CrossRef](#)]
66. Kashchiev, D.; van Rosmalen, G.M. Review: Nucleation in solutions revisited. *Cryst. Res. Technol.* **2003**, *38*, 555–574. [[CrossRef](#)]
67. Forjanés, P.; Astilleros, J.M.; Fernández-Díaz, L. The formation of barite and celestite through the replacement of gypsum. *Minerals* **2020**, *10*, 189. [[CrossRef](#)]
68. Ruiz-Agudo, E.; Putnis, C.; Putnis, A. Coupled dissolution and precipitation at mineral–fluid interfaces. *Chem. Geol.* **2014**, *383*, 132–146. [[CrossRef](#)]
69. Sabo, M.; Beckingham, L. Porosity—Permeability evolution during simultaneous mineral dissolution and precipitation. *Water Resour. Res.* **2021**, *57*, 59. [[CrossRef](#)]
70. Hommel, J.; Coltman, E.; Class, H. Porosity—Permeability relations for evolving pore space: A review with a focus on (bio-)geochemically altered porous media. *Transp. Porous Media* **2018**, *124*, 589–629. [[CrossRef](#)]
71. Kang, Q.; Chen, L.; Valocchi, A.; Viswanathan, H. Pore-scale study of dissolution-induced changes in permeability and porosity of porous media. *J. Hydrol.* **2014**, *517*, 1049–1055. [[CrossRef](#)]
72. Liu, M.; Mostaghimi, P. Characterisation of reactive transport in pore-scale correlated porous media. *Chem. Eng. Sci.* **2017**, *173*, 121–130. [[CrossRef](#)]
73. Meulenbroek, B.; Farajzadeh, R.; Bruining, H. Process-based upscaling of reactive flow in geological formations. *Int. J. Heat Mass Transf.* **2020**, *157*, 119969. [[CrossRef](#)]
74. Lin, W.; Li, X.; Yang, Z.; Lin, L.; Xiong, S.; Wang, Z.; Wang, X.; Xiao, Q. A new improved threshold segmentation method for scanning images of reservoir rocks considering pore fractal characteristics. *Fractals* **2018**, *26*, 1840003. [[CrossRef](#)]
75. Lin, W.; Xiong, S.; Liu, Y.; He, Y.; Chu, S.; Liu, S. Spontaneous imbibition in tight porous media with different wettability: Pore-scale simulation. *Phys. Fluids* **2021**, *33*, 32012. [[CrossRef](#)]
76. Jeroen, S.; Steffen, B.; Keschma, G.; Niels, B.; Gdanski, R. Experimental and numerical investigation of wormholing during CO₂ storage and water alternating gas injection. *Int. J. Greenh. Gas Control* **2020**, *94*, 102901.
77. Ruiz-Agudo, C.; Putnis, C.V.; Ruiz-Agudo, E.; Putnis, A. The influence of pH on barite nucleation and growth. *Chem. Geol.* **2015**, *391*, 7–18. [[CrossRef](#)]